Supporting information for: "Closure study of aerosol-stratocumulus interactions with UCLALES-SALSA during the Puijo 2020 campaign"

Silvia M. Calderón[1], Juha Tonttila[1], Angela Buchholz[2], Jorma Joutsensaari[2], Mika Komppula[1], Ari Leskinen[1,2], Liqing Hao[2], Dmitri Moisseev[3,4], Iida Pullinen[2], Petri Tiitta[1], Jian Xu[5], Annele Virtanen[2], Harri Kokkola[1], and Sami Romakkaniemi[1]

[1]Atmospheric Research Centre of Eastern Finland, Finnish Meteorological Institute, P.O. Box 1627, 70211 Kuopio, Finland
[2]Department of Applied Physics, University of Eastern Finland
[3]Institute for Atmospheric and Earth System Research/Physics, Faculty of Science, University of Helsinki, Helsinki, Finland
[4]Finnish Meteorological Institute, Helsinki, Finland
[5]Institute of Energy and Climate Research, IEK-8: Troposphere, Forschungzentrum Jülich GmbH, 52425 Jülich, Germany

Correspondence: S. Calderón (silvia.calderon@fmi.fi)

This document contains additional information about the modelling closure study of aerosol-interactions using UCLALES-SALSA and in-cloud observations from the Puijo 2020 campaign. The information is organized as follows:

1. UCLALES-SALSA modelling framework
2. Instrumentation used during the Puijo 2020 campaign
3. Description of cloud cases
4. Aerosol properties
5. Variability of cloud properties and cloud radar observations
6. Temperature and net radiative flux profiles
7. Vertical wind distributions
8. Cloud droplet activation and activation efficiency curves
9. Model sensitivity analysis to inputs related to aerosol mixing state in simulations of Case 1
10. Cloud microphysics and derived quantities
11. Emulation of the radar Doppler velocity

1 Modelling framework of UCLALES-SALSA

Table S1 describes the modelling framework used by UCLALES-SALSA to represent aerosol-hydrometeors interactions.

Table S1. Modelling framework of microphysical processes in UCLALES-SALSA

Process	Description	Modelling technique	Reference
Nucleation*	Aerosol formation	Activation-type nucleation above critical nuclei diameter	Kokkola et al. (2008)
Condensation	Water condensation on activated droplets Condensation of aerosol gas precursors	Analytical predictor of condensation scheme	Kokkola et al. (2008) based on Jacobson (2005)
Coagulation (collision-coalescence)	Brownian coagulation Convective enhanced Brownian coagulation Gravitational collection	Semi-implicit method	Tonttila et al. (2017) based on Jacobson (2005)
Hydration	Aerosol water uptake	Zdanovskii-Stokes-Robinson rule	Stokes and Robinson (1966)
Droplet activation or deactivation	Formation of cloud droplet or formation of interstitial aerosol	Activation if droplet is above critical size Deactivation	Tonttila et al. (2017)
Autoconversion	Formation of precipitation droplets by cloud droplet interaction	Treated as coagulation after cloud droplet collision	Tonttila et al. (2021) based on Jacobson (2005)
Accretion	Growth of precipitation droplets by collection of cloud droplets	Treated as coagulation by gravitational collection	Tonttila et al. (2021) based on Jacobson (2005)
Aerosol scavenging	Collection of aerosol particles by cloud and precipitation droplets	Treated as coagulation after particle-droplet collision	Tonttila et al. (2017) based on Jacobson (2005)
Precipitation	Sedimentation of precipitation droplets	Gravitational settling as defined by terminal velocity	Tonttila et al. (2017)
Ice formation	Immersion freezing of supercooled cloud droplets containing insoluble core	Ice germ formation from liquid on insoluble solid substrate	Ahola et al. (2020) based on
	Homogeneous freezing of supercooled droplets with or without insoluble core	Homogeneous ice nucleation at T < -30 °C	Khvorostyanov and Sassen (1998)
	Deposition freezing on dry insoluble aerosol particles	Ice germ formation from vapor on insoluble solid substrate	Khvorostyanov and Curry (2000) Hoose et al. (2010)
	Contact freezing	Treated as immersion freezing after particle-droplet collision	Hoose et al. (2010)

[a] Not used in this study, but available in the model

2 Instrumentation used during the Puijo 2020 campaign

Table S2 summarizes details of the instrumentation used during the Puijo campaign 2020 to measure aerosol and droplet properties, as well as meteorological variables that are relevant to this study.

3 Description of cloud cases

4 Aerosol properties

Observations of aerosol composition during the Puijo 2020 campaign were carried out with an Aerosol Chemical Speciation monitor (ACSM) described by Ács et al. (1991) that measures bulk mass of chemical species in PM_1, and also with an Aerodyne high-resolution aerosol time-of-flight mass spectrometer (HR-ToF-AMS) described by DeCarlo et al. (2006), hereafter referred as AMS, that measures size-segregated concentrations for particles with sizes ranging from $40\,\mathrm{nm}$ to $1\,\mu\mathrm{m}$. Both instruments monitored the presence of sulfate, organic carbon, nitrate and ammonium in aerosol particles. Number and mass concentrations are reported in Table S4. During the campaign, ACSM was positioned in the Puijo station, at the top of the tower. It measured the aerosol samples from the total inlet line every twenty minutes. The AMS was located at ground level, c.a. 224 m below the Puijo station. The small difference in altitude between the ACSM and AMS sampling points leads us to assumed that measurements are originated from the same air parcel, i.e. mass size distributions derived from AMS are representative of observations at the Puijo station.

As concentrations of sulfate and organic carbon were significantly higher than those of nitrate and ammonium during the selected cloud events, we assumed that aerosol particles contain just sulfate and organic carbon with densities equal to $1830\,\mathrm{kg\,m^{-3}}$ (Kokkola et al., 2008) and $1320\,\mathrm{kg\,m^{-3}}$, respectively. Properties for organic carbon were assumed to be similar to those of monosaccharide derivatives from the pyrolysis of cellulose and common tracers of biomass burning emissions such as levoglucosan, mannosan and galactosan, a polymeric form of galactose (Simoneit et al., 1999; Parshintsev et al., 2017) with molar mass values of $162.1406\,\mathrm{g\,mol^{-1}}$, $180.14\,\mathrm{g\,mol^{-1}}$ and $180.1559\,\mathrm{g\,mol^{-1}}$ and density values as pure solid species of $1630\,\mathrm{kg\,m^{-3}}$, $1700\,\mathrm{kg\,m^{-3}}$ and $1500\,\mathrm{kg\,m^{-3}}$, respectively (Linstrom and Eds., 2017; Royal Society of Chemistry, 2015). Similar properties correspond to tracers of biogenic organic emissions such as glucose, arabitol and mannitol (Samaké et al., 2019) with molar mass values of $180.1559\,\mathrm{g\,mol^{-1}}$, $152.1458\,\mathrm{g\,mol^{-1}}$ and $182.1718\,\mathrm{g\,mol^{-1}}$ and density as pure solids of $1600\,\mathrm{kg\,m^{-3}}$, $1500\,\mathrm{kg\,m^{-3}}$ and $1520\ \mathrm{kg\,m^{-3}}$, respectively (Linstrom and Eds., 2017; Royal Society of Chemistry, 2015). Dust grain density values range between $2100\,\mathrm{kg\,m^{-3}}$ and $2690\,\mathrm{kg\,m^{-3}}$ (Rocha-Lima et al., 2018), but a value of $2650\,\mathrm{kg\,m^{-3}}$ is typically used to parameterize dust properties in modelling frameworks (Mahowald et al., 2014; Rocha-Lima et al., 2018). Dust composition in highly variable but comprises minerales such as hematite, kaolinite, illite montmorillonite, quartz and calcite (Balkanski et al., 2007).

UCLALES-SALSA can represent an externally mixed aerosol population composed of two different particle regimes. Aerosol properties for each regime are initialized using the number size distribution and the chemical composition in volume fraction, as it is assumed that all particles in a single regime have the same composition with a particle density that is

Table S2. Instrumentation used during the Puijo 2020 campaign relevant to this study

Parameter(s)	Detection principle	Instrument	Measurement range	Acquisition time	Additional information
Aerosol (interstitial and total) size distribution	Twin-inlet DMPS system: total inlet (D<40 µm), interstitial (D<1 µm)	Differential Mobility Particle Sizer (DMPS)	3 nm - 800 nm 76 size bins	12 min	Portin et al. (2014); Väisänen et al. (2016)
Cloud and precipitation droplet size distribution, liquid water content	Light scattering at 680 nm	Forward-scattering optical spectrometer	3 µm - 50 µm 30 size bins	5 s	Spiegel et al. (2012)
Cloud and precipitation droplet size distribution, liquid water content	Digital holographic imaging	Optical cloud droplet and ice crystal measurement system ICEMET	5 µm - 200 µm 195 size bins	60 s	Kaikkonen et al. (2020)
Aerosol mass concentration and chemical composition	Mass spectrometry after high vacuum thermal particle vaporization and electron impact ionization	Aerosol Chemical Speciation Monitor (ACSM)		20 min	Ng. et al. (2011)
Size-segregated aerosol mass concentration	Mass spectrometry after high vacuum thermal particle vaporization and electron impact ionization	Aerosol Mass Spectrometer (AMS)		5 min	DeCarlo et al. (2006)
Cloud base height	Backward light scattering at 908 nm	Laser ceilometer	15 m- 7500m	15-120 s	Markowicz et al. (2008)
Cloud base height and Cloud top height Vertical wind distribution	Light scattering coefficient at 2.7 mm - 4mm	Millimeter-wave cloud radar			Küchler et al. (2017)
Elastic backscattering coefficient vertical wind at cloud base	Light scattering at 1.55 µm	Doppler lidar		30s	Tucker et al. (2009) (Hirsikko et al., 2014) (Manninen et al., 2018)

Table S3. Cloud properties and meteorological parameters during selected cloud events measured at the Puijo top monitoring site. Values are reported as arithmetic mean, [25th, 50 th, 75 th] percentiles, (number of observations)

Cloud event	24 September 2020	31 October 2020
Cloud properties		
Time, UTC+02:00	07:54 - 12:49	00:35 - 06:35
Duration (h)	4.9	6.0
Number of cloud layers	1	1
Water phases	Liquid	Liquid, solid
[b] Retrieved cloud base height [m]	63, [30, 60, 90], (296),	122,[90,120,150], (326)[b]
[c] Retrieved cloud top height [m]	260, [153, 302, 343], (6436)	457,[435,460,486], (5588)
Meterological conditions (based on 1-min average values)		
Temperature [K]	283.55,[283.25,283.35,283.95], (295)	270.80, ,[270.55,270.75,270.95], (326)
Relative humidity [%]	95.8,[95.2,96.0,96.7], (295)	94.3, [93.3,94.2,95.2], (326)
Wind speed [$\mathrm{m\,s^{-1}}$]	6.3,[5.8,6.3,6.7], (295)	3.4, ,[3.8,3.9,4.0], (326)
Wind direction [degrees]	178.2,[172.6,176.8,182.5], (295)	183.4 ,[128.2,317.0,359.8], (326)
VIS1 [m]	57,[44,48,53], (295)	125 ,[100,112,136], (426)

[a] Halo Doppler lidar [b] Ceilometer, [c] Cloud radar

equal to the material density. Following the definition of material density, it is assumed that there is no void space or change in particle volume upon mixing of aerosol constituent. Thus, each compound adds to the total particle volume a volume equal to its volume as "pure" species (DeCarlo et al., 2004; Hu et al., 2012). The material density can be calculated in different forms depending on the data that is available, in our case if we used observations of the ACSM monitor, the material density is given as

$$\rho_m = \frac{\sum_i w_i}{\sum_i \frac{w_i}{\rho_i}}, \tag{1}$$

where w_i is the bulk mass concentration of species i for aerosol particles with mobility diameter below 1 µm or PM_1 as measured by the ACSM monitor and ρ_i is the density of species i in solid state.

This material density can be later used to calculate the volumetric fraction of species i in every aerosol particle ϕ_i as

$$\phi_i = \frac{\rho_m}{\sum_i w_i} \frac{w_i}{\rho_i}. \tag{2}$$

However, when the aerosol composition can be retrieved from both, AMS and ACSM measurements, we must iterate the ϕ_i values for both aerosol constituents until two conditions are satisfied. First, size-segregated mass concentrations derived from aerosol number concentrations obtained with the DMPS monitor must be in close agreement to average values for the cloud event measured with the AMS monitor (3a). Second, the cumulative mass in particles with mobility diameter below 1 µm must

Table S4. Aerosol properties during selected cloud events measured at the Puijo top monitoring site. Values are reported as arithmetic mean, [25th, 50 th, 75 th] percentiles. N_{tot}, N_{acc} and N_{ait} are aerosol number concentrations in the total size range from 27 nm to 1000 nm, in the accumulation mode from 100 nm to 1000 nm and in the Aitken mode from 25 nm to 100 nm, respectively. CDNC represents droplet number concentration retrieved from Twin-inlet DMPS system measurements

Cloud event	24 September 2020	31 October 2020
	Aerosol size distribution[e]	
Number of measurements	5	8
N_{tot} [cm^{-3}]	2042, [1932, 2093, 2119]	201, [76, 135, 282]
N_{ait} [cm^{-3}]	633, [564,626,695],(5)	108, [32,64,142],(8)
N_{acc} [cm^{-3}]	1347, [1310,1343,1376]	86, [43,69,131]
$N_{\mathrm{acc}}/N_{\mathrm{tot}}$	0.66, [0.64,0.67,0.68]	0.49, [0.44,0.53,0.55]
$N_{\mathrm{ait}}/N_{\mathrm{acc}}$	0.47, [0.43,0.44,0.52]	1.05, [0.79,0.83,1.2]
CDNC [f] [cm^{-3}]	687, [611,728,797]	103, [44,73,146]
D_{50} [µm]	0.167, [0.156,0.158,0.173]	0.097, [0.092, 0.096,0.104]
$N_{\mathrm{d}}/N_{\mathrm{tot}}$	0.34, [0.29,0.38,0.40]	0.54, [0.51,0.55,0.58]
	Aerosol composition[g]	
PM_1 $\mu\mathrm{g\,m}^{-3}$	13.7, [12.7,13.1,14.5], (14)	1.4, [1.0,1.4,1.8], (6)
PM_1-organic carbon $\mu\mathrm{g\,m}^{-3}$	7.5, [7.1, 7.4, 7.7], (14)	0.2, [0.1, 0.2, 0.3], (6)
PM_1-sulphate $\mu\mathrm{g\,m}^{-3}$	3.9, [3.5, 3.7, 3.9], (14)	0.8, [0.7, 0.8, 1.0], (6)
PM_1-nitrate $\mu\mathrm{g\,m}^{-3}$	0.8, [0.7, 0.7, 0.8], (14)	0.06, [0.05, 0.07, 0.08], (6)
PM_1-ammonium $\mu\mathrm{g\,m}^{-3}$	1.6, [1.2,1.6,2.0], (14)	0.4, [0.1, 0.3, 0.6], (6)

[e] Twin-inlet differential mobility particle sizer, total inlet[f] calculated as the concentration difference between the total and interstitial lines (Portin et al., 2014)

[g] Aerosol Chemical Speciation Monitor (ACSM)

be close to the bulk mass in PM_1 measured by the ACSM (3b). These conditions can be expressed as

$$w_{i,\mathrm{AMS}}\left(D_m\right) = \rho_i \phi_i \frac{\pi}{6} D_m^3 n\left(D_m\right) dD_m \tag{3a}$$

and

$$W_{i,\mathrm{ACSM}} = \int^{1\mu m} w_i\left(D_m\right) dD_m = \int^{1\mu m} \rho_i \phi_i \frac{\pi}{6} D_m^3 n\left(D_m\right) dD_m, \tag{3b}$$

where D_m is the particle mobility diameter, $n\left(D_m\right)$ and $w_{i,\mathrm{AMS}}\left(D_m\right)$ are the number concentration and the mass concentration of species i in aerosol particle with mobility diameter equal to D_m and $W_{i,\mathrm{ACSM}}$ is the mass concentration of species i in particles with mobility diameter below 1 µm. It is important to highlight that AMS-size distributions were transformed from vacuum aerodynamic diameter to mobility diameter by means of the estimated material density assuming that particles are spherical after disregarding slip correction factors.

The calculation of the dry-volume based composition changes if we assume that the aerosol population is externally mixed with particles existing in two different mixing states, A and B, both with the same size-segregated number concentration obtained from DMPS measurements. In this case, we must also iterate the fraction of particles existing in each regime, as well as the volumetric fraction of aerosol constituents in each one of them until the restrictions in total number concentrations and total mass concentration are satisfied as follows

$$w_{i,\mathrm{AMS}}\left(D_m\right) = F_A\left(\rho_i \phi_{i,A} \frac{\pi}{6} D_m^3 n\left(D_m\right) dD_m\right) + F_B\left(\rho_i \phi_{i,B} \frac{\pi}{6} D_m^3 n\left(D_m\right) dD_m\right), \tag{4a}$$

$$W_{i,\mathrm{ACSM}} = \int^{1\mu m} F_A\left(\rho_i \phi_{i,A} \frac{\pi}{6} D_m^3 n\left(D_m\right) dD_m\right) + \int^{1\mu m} F_B\left(\rho_i \phi_{i,B} \frac{\pi}{6} D_m^3 n\left(D_m\right) dD_m\right) \tag{4b}$$

and

$$F_A + F_B = 1, \tag{4c}$$

where F_A and F_B are the fraction of the total number of aerosol particles in regimes A and B, while $\phi_{i,A}$ and $\phi_{i,B}$ represent the volumetric fraction of species i in regimes A and B, respectively.

To assess the effect of the aerosol mixing state in our simulations for case 1, we used two different settings of aerosol properties. In the first, we studied an internally mixed aerosol population that was initialized with volumetric fraction values of 74.5% v/v and 25.5 % v/v for organic carbon and sulfate, respectively. In the second scenario, we switched to an externally mixed aerosol population composed by two regimes, regime A representing 66.7% of the total number of aerosol particles, and regime B representing the remaining 33.3%. Aerosol particles in regime A were composed of 65% v/v organic carbon and 35%v/v sulfate; while those in regime C contained 97% v/v organic carbon and 3%v/v sulfate. We show estimated concentrations per event hour as well as the average for the whole event. The fraction of the total number of aerosol particles in each regime was iterated after there was a close agreement for sulphate concentrations (i.e. the dashed-line representing the average-model-mass-size distribution and the continuous line representing the hourly-average mass size distribution found by AMS observations). As it can be noticed in Figure S1 and Figure S2 sulfate concentrations from observations match closely average estimated values, while organic carbon concentrations behave in the opposite way. It was very difficult to find perfect agreements for both chemical species. Convergence criteria for iterations used sulfate, the most hygroscopic compound, since it must have the strongest influence on cloud droplet activation and droplet growth. Total mass concentrations of sulfate and organic carbon used in both simulations are equivalent between them.

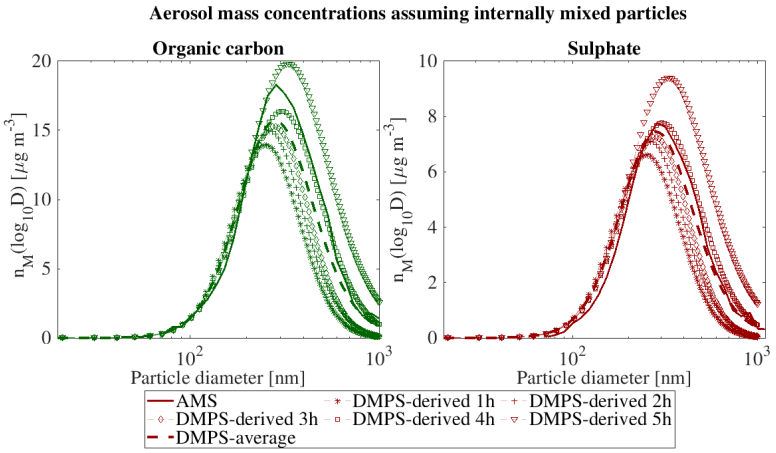

Figure S1. Comparison of size segregated aerosol mass concentrations used in simulation initialized with an internally mixed aerosol population for the cloud event of 24 September 2020

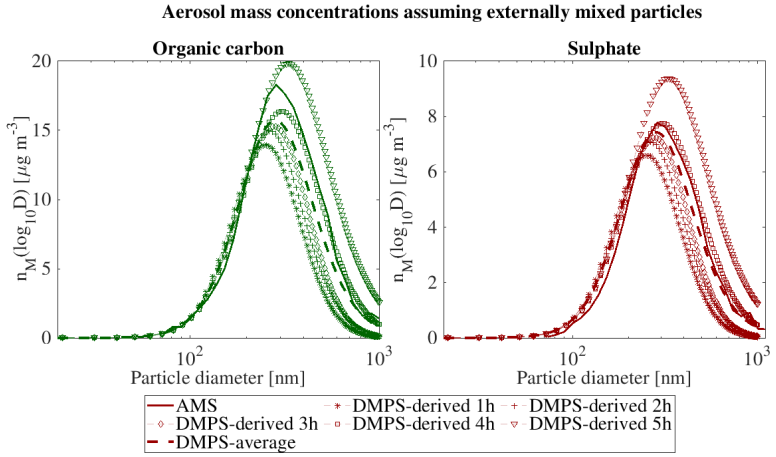

Figure S2. Comparison of size segregated aerosol mass concentrations used in simulation initialized with an externally mixed aerosol population for the cloud event of 24 September 2020

Similar calculations were performed to find the aerosol composition in Case 2. For our simulations in level 4 (liquid droplets) we used a dry volume-based composition of 88%v/v organic carbon and 12% v/v sulfate, both with the same shape of the aerosol size distribution. The simulation in level 5 that includes ice formation was performed with an externally mixed aerosol population where 85% of the total aerosol loading was in regime A with 88%v/v organic carbon and 12% v/v sulfate; and the remaining 15% of the total aerosol number concentration was in regime B with a composition equal to 90.5% v/v sulfate and 9.5%v/v dust. The percentage of particles and composition of regime B was chosen to give the best representation of observed droplet size distributions among different simulation scenarios.

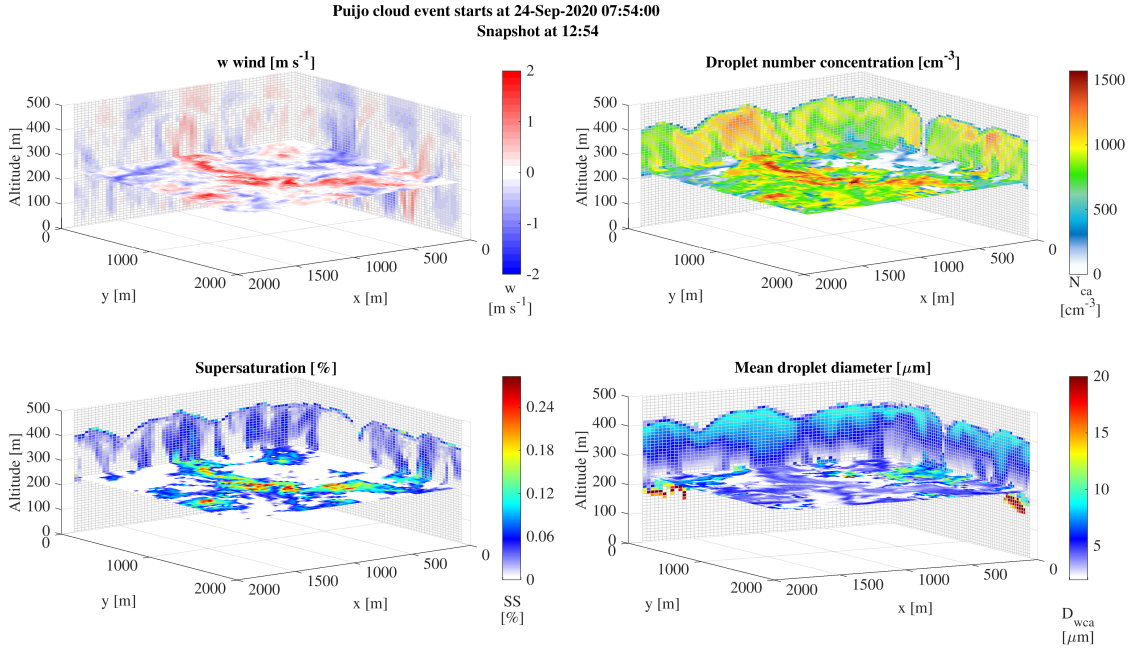

Figure S3. Variability of stratocumulus-capped boundary layer properties during the cloud case 1 as modelled by UCLALES-SALSA across lateral surfaces of model domain as well as the horizontal plane at 225 m of altitude corresponding to Puijo top monitoring site. Color scales reflect 1-minute values of a) vertical wind velocity b) supersaturation c) cloud droplet number concentration d) count median wet diameter of cloud droplets

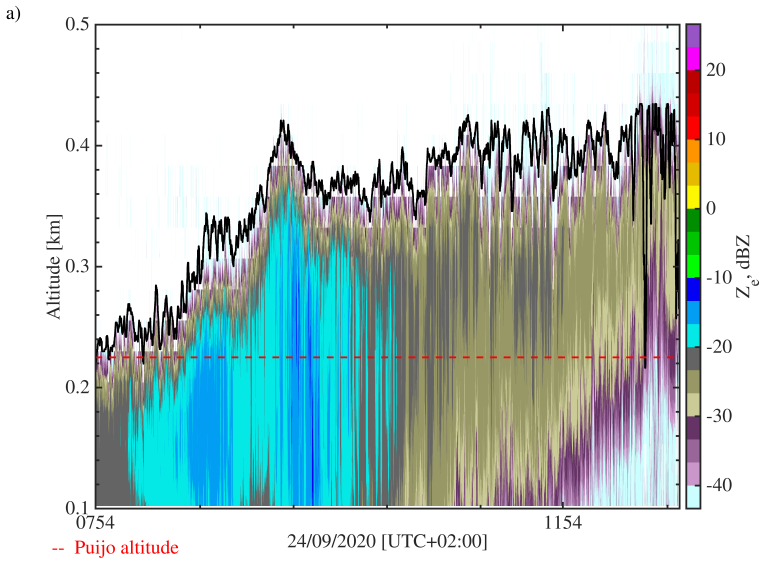

Figure S4. Cloud top retrieved from observations of the millimeter-wave cloud radar located at the Savilahti station for the diurnal cloud case of 24 September 2020

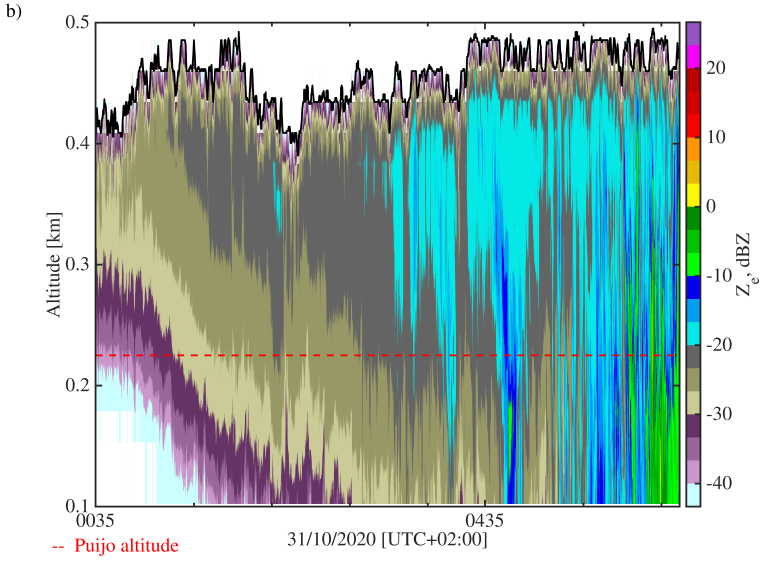

Figure S5. Cloud top retrieved from observations of the millimeter-wave cloud radar located at the Savilahti station for the nocturnal cloud case of 31 October 2020

6 Temperature and net radiative flux profiles

Stratocumulus capped boundary layers have two distinctive features that correlate to each other, the convective instability driven by cloud top longwave radiative cooling and the temperature inversion immediately above cloud top that is maintained by the former (Wood, 2012). The strength and temporal variation of the inversion temperature can be seen in Figure S6.1 for Case 1, and in Figure S7.1 for Case 2. Time series of 1-min resolution and probability distributions of cloud top radiative cooling rates simulated with UCLALES-SALSA are shown in Figure S8 for Case 1 and in Figure S9 for Case 2.

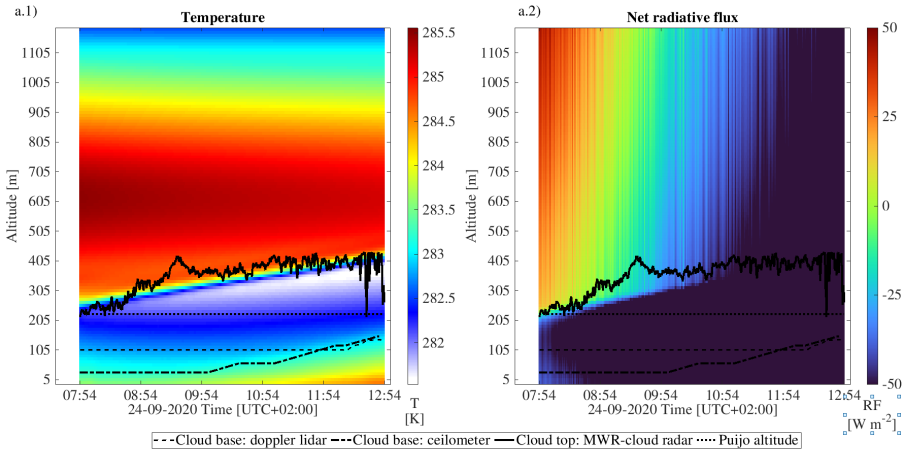

Figure S6. Vertical profiles of temperature and net radiation flux calculated by UCLALES-SALSA for the diurnal cloud case of 24 September 2020

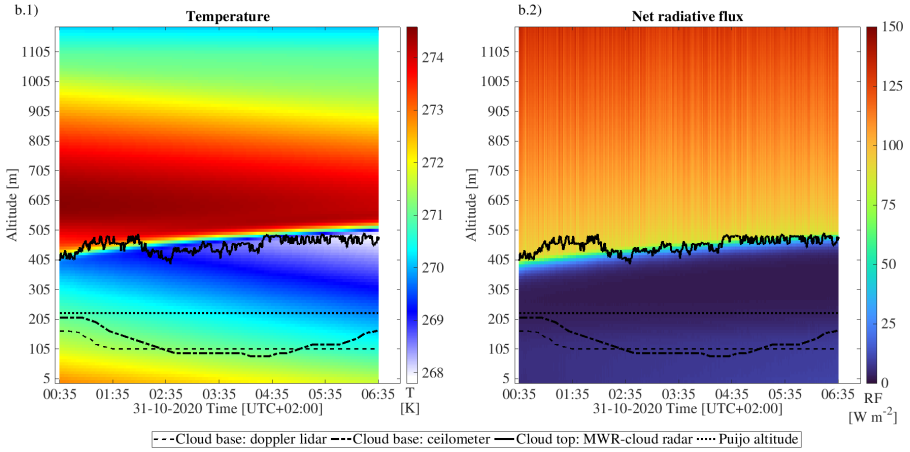

Figure S7. Vertical profiles of temperature and net radiation flux calculated by UCLALES-SALSA for the nocturnal cloud case of 31 October 2020

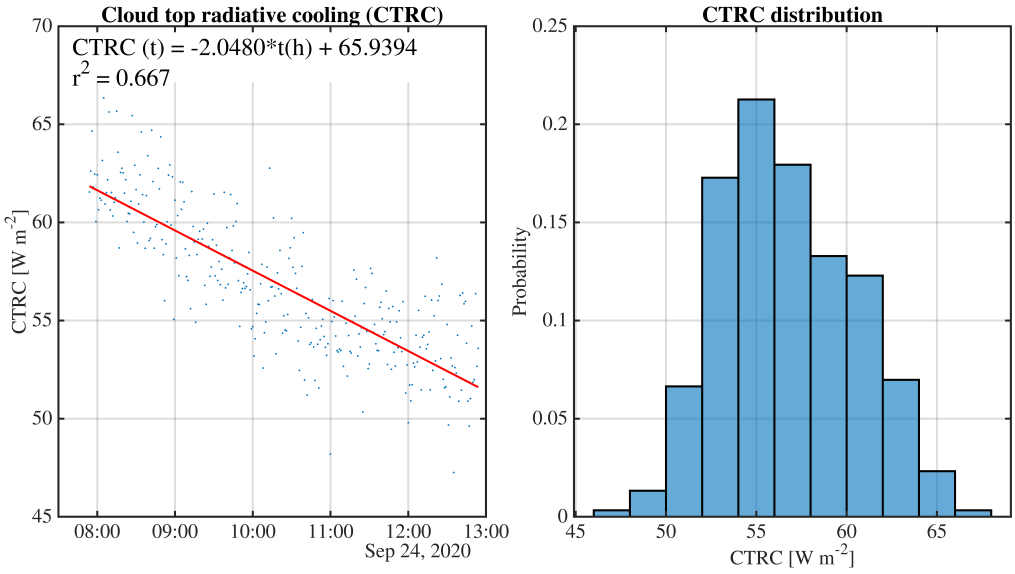

Figure S8. Cloud top radiative cooling calculated by UCLALES-SALSA for the diurnal cloud case of 24 September 2020. Left panels: 1-min time series. Right panels: probability distribution for the event.

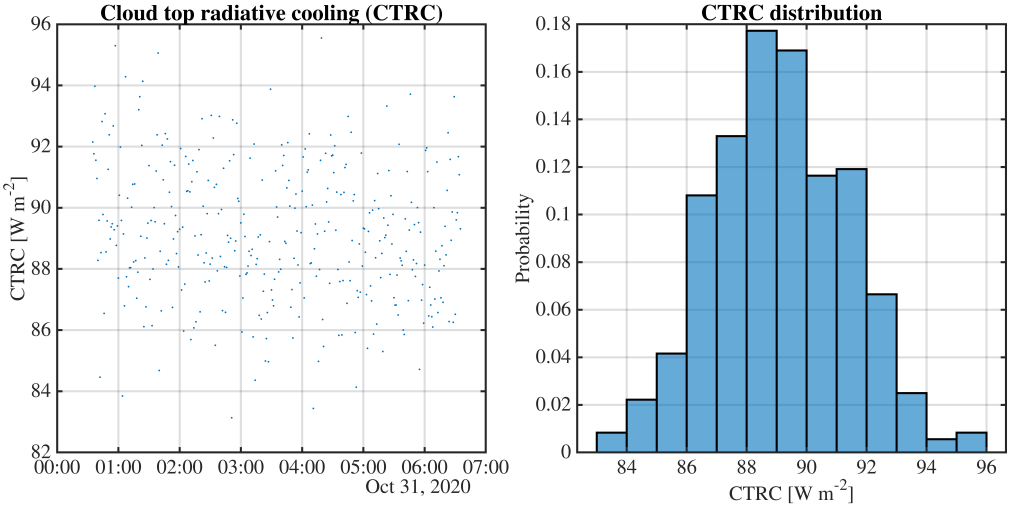

Figure S9. Cloud top radiative cooling calculated by UCLALES-SALSA for the nocturnal cloud case of 31 October 2020. Left panels: 1-min time series. Right panels: probability distribution for the event.

]

7 Vertical wind distribution

The intensity of turbulence was characterized by the variance of the distribution of vertical wind velocity calculated for hourly intervals as

$$\sigma_w^2(z) = \frac{\sum_{xy}(w - \bar{w})^2}{N}, \tag{5}$$

where w is the vertical wind velocity at every grid point of the horizontal domain at an specific altitude z, $\bar{w}$ is the mean value of the vertical wind for all N values in the hourly interval.

Figure S10 and Figure S11 compile distributions of the vertical wind velocity modeled with UCLALES-SALSA and retrieved from observations of the Halo Doppler lidar at altitudes equivalent to the cloud base for each studied case. The degree of modelling closure is proportional to the overlapping area between histograms as it represents the amount of information shared by model-based and observation-based distributions.

The overlapping index (OVL) between two different probability distributions describing the behaviour of the same variable x is defined as

$$\mathrm{OVL} = \int min\left[f_1(x), f_2(x)\right] dx = \sum min\left[p_1(x), p_2(x)\right], \tag{6}$$

where x is the studied variable, in our case, the vertical wind velocity, $f_1(x)$ and $f_2(x)$ are the probability density functions (pdf) and $p_1(x)$ and $p_2(x)$ are probability distributions of the vertical wind velocity based on observations and modeled by UCLALES-SALSA, respectively (Inman and Bradley Jr., 1989).

During case 1 the modeled standard deviation of the vertical wind at cloud base increases along hourly intervals when solar radiation strengthens positive buoyancy caused by surface fluxes. During case 2, there are no significant changes in the modeled standard deviation of the vertical wind at cloud base, since the turbulence intensity in nocturnal cloud is controlled by cloud-top processes. In both cases, there is a good agreement between model results and observations despite the fact that values of cloud base height were close to the minimum altitude that can be scanned effectively by the lidar, approximately $100\,\mathrm{m}$, the radar is $87\,\mathrm{m}$ above ground level and the vertical resolution is $30\,\mathrm{m}$, approximately (Hirsikko et al., 2014).

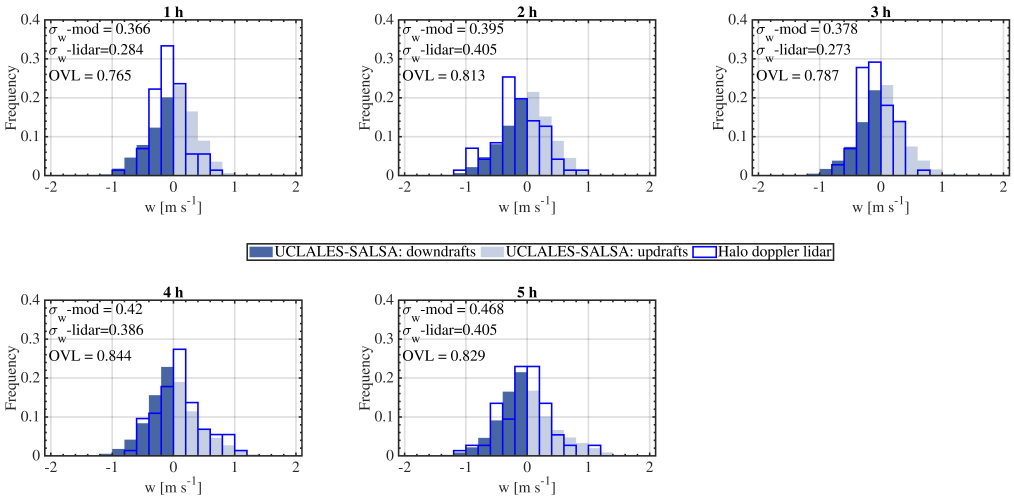

Figure S10. Histograms of vertical wind velocity observed with the Halo Doppler lidar and calculated with UCLALES-SALSA during hourly periods of Case 1 24 September 2020

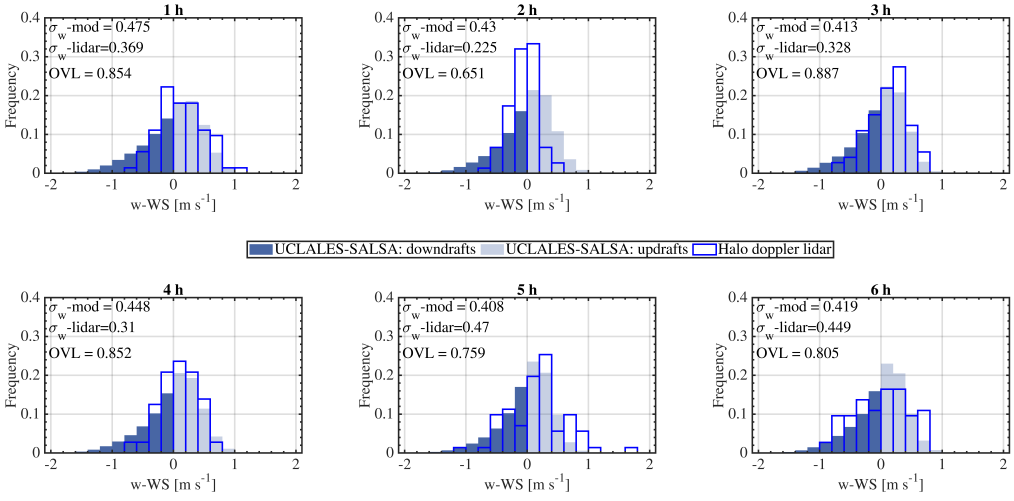

Figure S11. Histograms of vertical wind velocity observed with the Halo Doppler lidar and calculated with UCLALES-SALSA during hourly periods of Case 2, 31 October 2020

The modelling closure for vertical wind velocities along the cloud domain was based on observations of the cloud radar. Unlike Doppler lidars, cloud radars operate in the Rayleigh regime and their signals are more sensitive to larger droplets, e.g. cloud droplets with diameters between 10 µm to 100 µm give significantly lower signals compared to precipitation droplets or ice particles on the size range of 100 µm to 10 mm (Bühl et al., 2015). Due to the longer operating wavelength than used in lidars, cloud radars penetrate efficiently through cloud providing information from different cloud layers.

Model outputs for vertical wind are compared to cloud radar observations for hour-long periods in Figure S12, and in Figure S13 and Figure S14 at different altitudes ranging from cloud base height and cloud top height, respectively. Every panel in these figures shows the calculated standard deviation of the vertical wind from both, observations and model results, as well as the corresponding overlapping index to measure the degree of similarity between them. Frequencies of updraft and downdrafts wind calculated by UCLALES-SALSA are in good agreement with radar observations in terms of maximum values, variance and skewness of the wind distributions. The event-average overlapping index is 0.8620 ± 0.06 which indicates a strong similarity between distribution, and therefore, a good degree of modelling closure. This is an essential requisite to guarantee that modeled supersaturation values inside the cloud domain are representative of real in-cloud conditions. By comparison of panels in Figure S13 and Figure S14 we can notice that during the diurnal cloud event maximum updraft velocities are below $1\,\mathrm{m\,s^{-1}}$ and also that the frequencies for updrafts velocities decrease from cloud base to cloud top. Distributions become narrower at higher altitudes indicating weaker turbulence at upper cloud sections compared to the lower half of the cloud. This suggests that surface fluxes of heat and moisture are driving the turbulence structure inside the cloud. Distributions become broader at all altitudes as the time passes indicating that the intensity of turbulence increases along the cloud domain.

Distributions of vertical wind during the nocturnal cloud event of 31 October 2020 are shown in Figure S15 and Figure S16 for a range of altitudes between cloud base and cloud top. Updraft winds are weaker compared to those observed during the diurnal cloud event and are in the order of $0.6\,\mathrm{m\,s^{-1}}$. During the first three hours of the cloud event, the distributions of the modeled vertical wind agree reasonably well to observations in terms of frequency, variance and skewness at all altitudes. Drizzle formation and the occurrence of precipitation during the cloud event produce negatively skewed distributions in histograms of model outputs and observations. During precipitation the cloud radar signal is mainly dominated by larger falling hydrometeors (Bühl et al., 2015) becoming blind to small droplets carried up during updrafts. This explains why the right sides of calculated and observed histograms do not match as they did previously. The model tends to overestimate the updraft wind frequencies at the upper section of the cloud after the second hour because modelled velocities represent the air motion and do not consider directly the bulk sedimentation velocity of drizzle droplets, while radar velocities represent the vector sum of the air velocity and the reflectivity weighted settling velocity of all hydrometeors contained in the sampling volume. More information is included in Section I of this document. We have omitted the information about the overlapping index because it is not correct to compare different variables, so the degree of modelling closure is reported later in Section I in relation to distributions of the radar velocity.

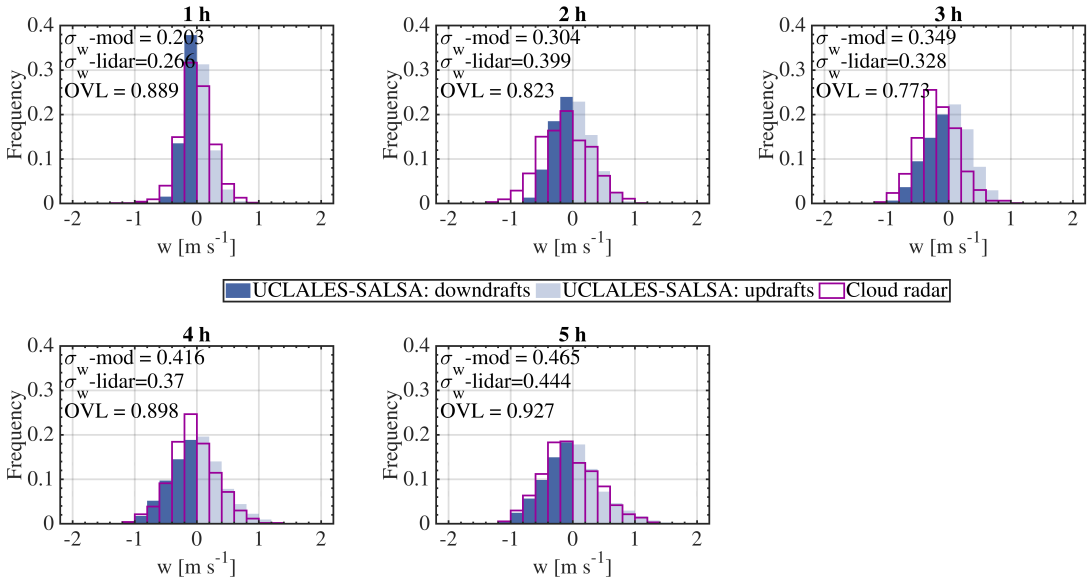

Figure S12. Hourly-average probability distribution of the vertical wind along the cloud domain observed with the cloud radar (Hydra-W radar) and calculated with UCLALES-SALSA for the diurnal cloud event on 24 September 2020

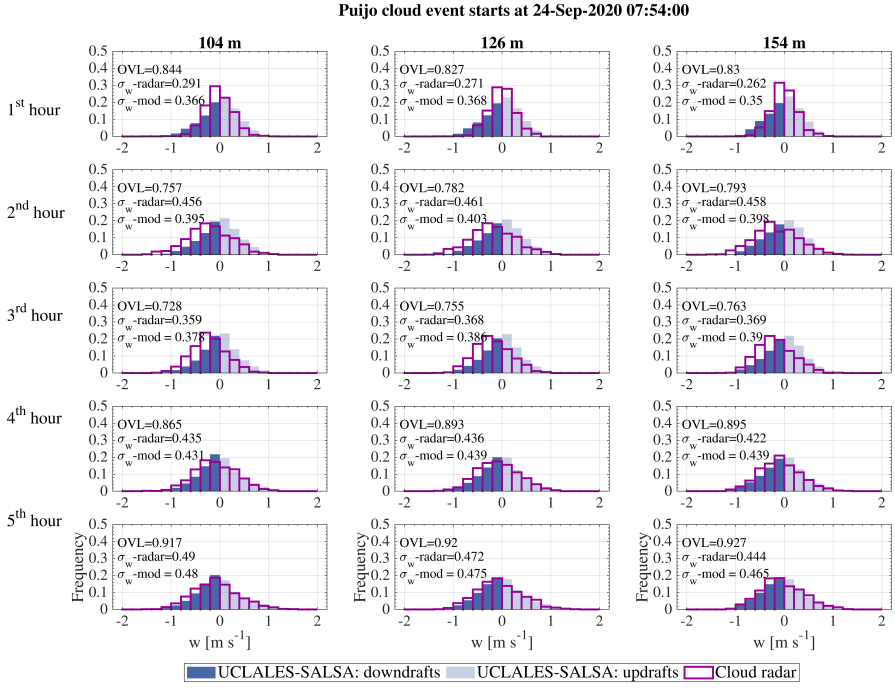

Figure S13. Probability distributions of vertical wind velocity observed with the cloud radar (Hydra-W radar) and calculated with UCLALES-SALSA for the diurnal cloud event on 24 September 2020 at the lower half of the cloud

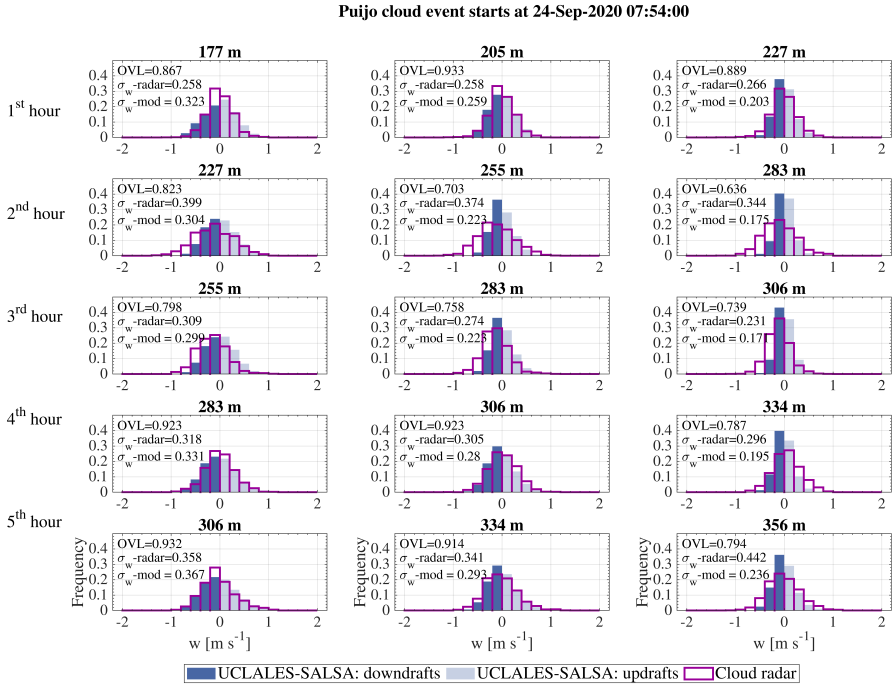

Figure S14. Probability distributions of vertical wind velocity observed with the cloud radar (Hydra-W radar) and calculated with UCLALES-SALSA for the diurnal cloud event on 24 September 2020 at the upper half of the cloud

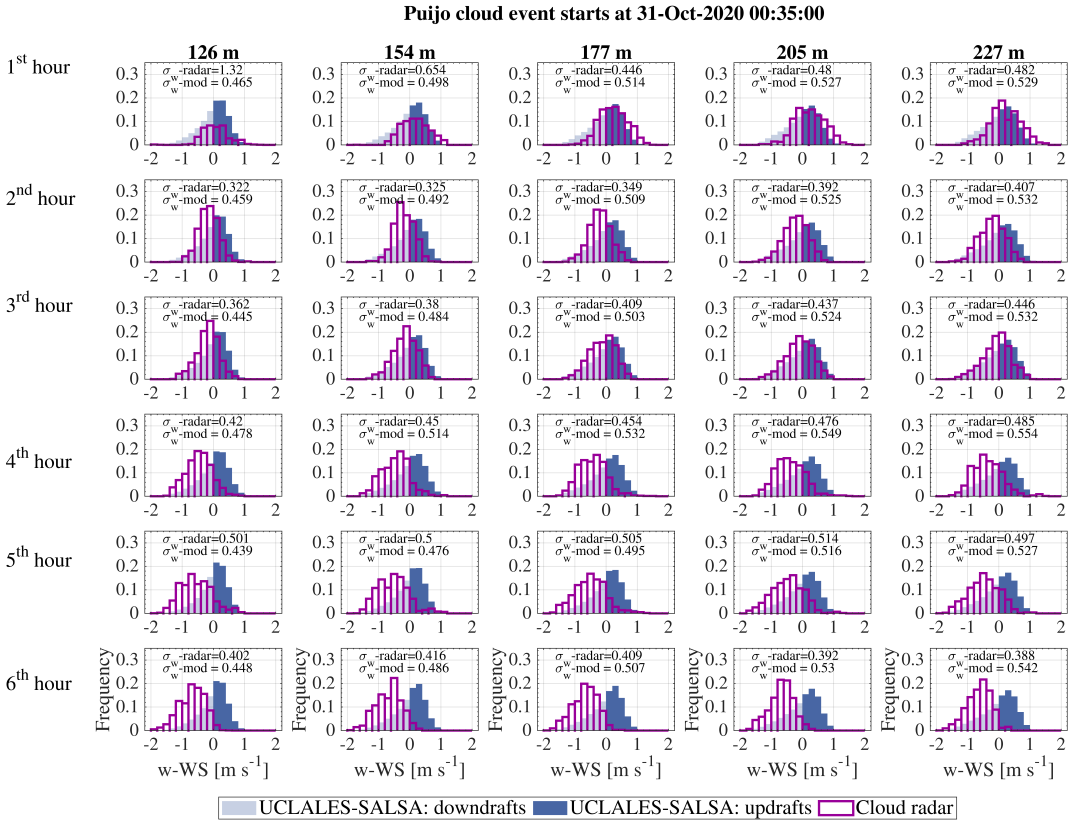

Figure S15. Probability distributions of vertical wind velocity observed with the cloud radar (Hydra-W radar) and calculated with UCLALES-SALSA for the nocturnal cloud event on 31 October 2020 at the lower section of the cloud

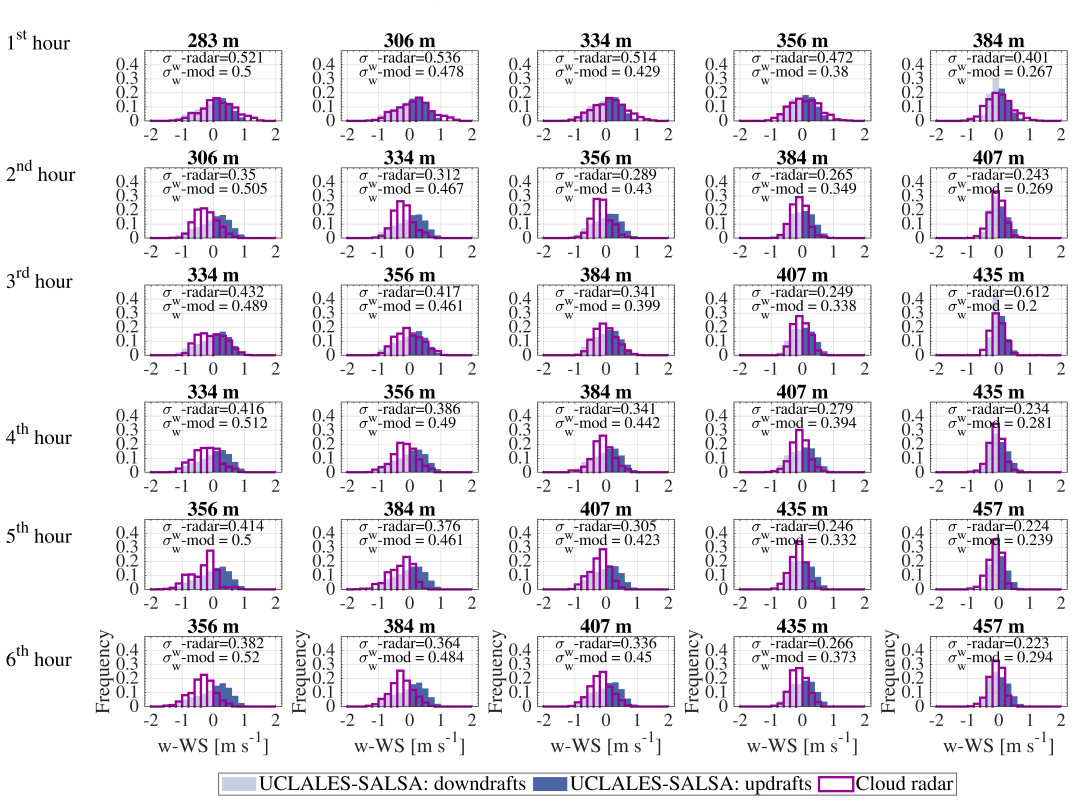

Figure S16. Probability distributions of vertical wind velocity observed with the cloud radar (Hydra-W radar) and calculated with UCLALES-SALSA for the nocturnal cloud event on 31 October 2020 at the upper section of the cloud

8 Cloud droplet activation and activation efficiency curves

The number concentration of activated droplets is experimentally measured as the difference between droplet number concentrations measured in the total and interstitial lines of the Twin-inlet differential mobility particle sizer system (Twin-inlet DMPS system). Cutoff diameter in the total inlet is ca. 40 µm which guarantees that the droplet number concentrations account for cloud droplets and also non activated or interstitial aerosol particles. Since the interstitial inlet is equipped with a PM_1 impactor which allows to collect just non activated aerosol particles, the activated fraction can be calculated as the ratio between number concentration of activated droplets and total droplet number concentrations for a certain dry particle size. More details about this sampling system can be found in literature (Portin et al., 2009, 2014).

In resemblance to experiments, number concentrations of activated droplets per size bin per altitude are calculated from model outputs in a two-step procedure. First, we calculate total number concentration of droplets with wet diameter below or

equal to 40 µm in size bin i as

$$N_{\mathrm{tot}}\left(D_{p,i},z,t\right)=\sum_{x}\sum_{y}N_{cba}\left(D_{p,i}z,x,y,t\right)\left(D_{wcba}\left(D_{p,i},z,x,y,t\right)\leq 40\mu\mathrm{m}\right)+$$
$$\sum_{x}\sum_{y}N_{pba}\left(D_{p,i},z,x,y,t\right)\left(D_{wpba}\left(D_{p,i},z,x,y,t\right)\leq 40\mu\mathrm{m}\right), \quad (7)$$

where $D_{p,i}$ is the dry particle mean diameter of size bin i, N_{cba} and N_{pba} are binned number concentration of cloud droplets and precipitation droplets, and D_{wcba} and D_{wpba} represent the wet diameter of cloud droplets and precipitation droplets, all of them referred to the dry size bin i. The inequality $\left(D_{wcba}\left(D_{p,i},z,x,y,t\right)\leq 40\mu\mathrm{m}\right)$ is an opposite binary variable that changes between one and zero if the condition is satisfied. Here, we have kept the variable nomenclature used in UCLALES-SALSA to facilitate the connection to current/future users of the model.

The number of non activated particles or interstitial particles in the size bin i is then calculated as

$$N_{\mathrm{int}}\left(D_{p,i},z,t\right)=\sum_{x}\sum_{y}N_{cba}\left(D_{p,i}z,x,y,t\right)\left(D_{wcba}\left(D_{p,i},z,x,y,t\right)\leq 1\mu\mathrm{m}\right)+$$
$$\sum_{x}\sum_{y}N_{pba}\left(D_{p,i},z,x,y,t\right)\left(D_{wpba}\left(D_{p,i},z,x,y,t\right)\leq 1\mu\mathrm{m}\right). \quad (8)$$

The number of activated droplets at altitude z in size bin i is then calculated as

$$N_{\mathrm{act}}\left(D_{p,i},z,t\right)=N_{tot}\left(D_{p,i},z,t\right)-N_{int}\left(D_{p,i},z,t\right). \quad (9)$$

The number of activated droplets is graphically depicted as the difference between blue and red areas in Figure S17 for Case 1 and Figure S18 for Case 2. Model-based number concentrations for total aerosol and interstitial aerosol are in good agreement with those measured with the Twin-inlet DMPS system as it is evidenced by overlapping indexes values above 0.82 in all cases. The modelling closure for Case 2 is not as optimal as it was for Case 1, especially at the last 3 hours of the cloud event. The best agreement was found for the simulation performed with 40% reduction in the initial aerosol loading including ice-related processes. In this case, the model could follow nicely the trend in the accumulation mode but overestimate number concentrations of the Aitken mode, almost immediately after the first hour. Possible causes of these biases could be related to underestimation of in-cloud scavenging rates during drizzle/ice formation, but also to experimental uncertainties since aerosol number concentrations are very low and close to detection limits of instruments.

Once, the number of activated droplet is calculated, it is possible to determine the activated fraction of aerosol particles at altitude z in size bin i as

$$f_{\mathrm{act}}\left(D_{p,i},z,t\right)=\frac{N_{\mathrm{act}}\left(D_{p,i},z,t\right)}{N_{\mathrm{tot}}\left(D_{p,i},z,t\right)} \quad (10)$$

CCN activation efficiency curves from experimental observations and model results are then represented using the cumulative sum of f_{act} as a function of dry particle diameter (Portin et al., 2014). We include here in Figure S19 the comparison between observation-based activation efficiency curves for Case 1 and those retrieved from model outputs in grid points with updrafts or downdraft. For Case 2, Figure S20 compares activation efficiency curves for the different simulation scenarios.

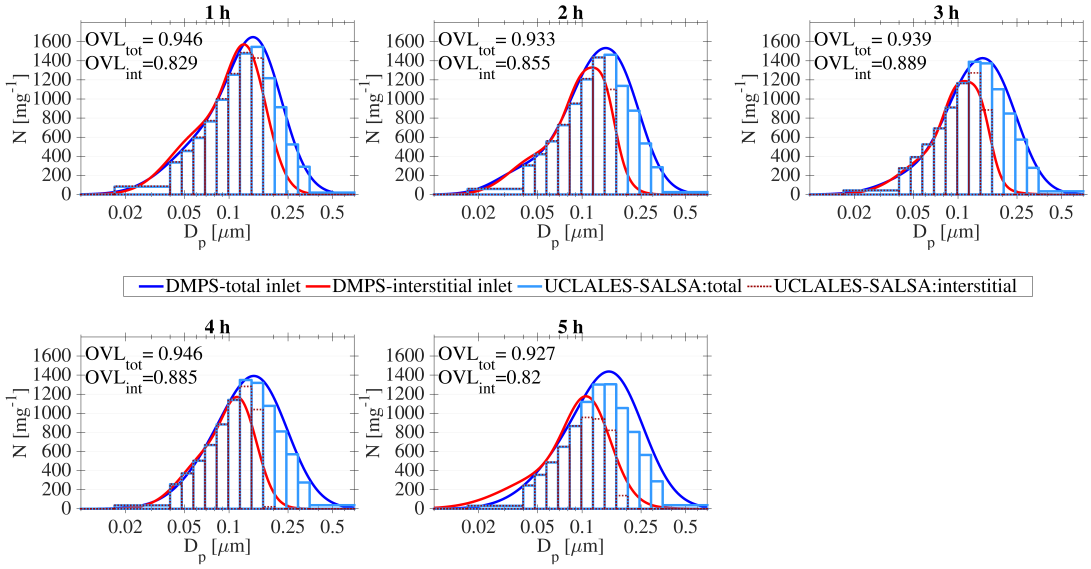

Figure S17. Aerosol size distributions measured with the Twin-inlet DMPS system at the Puijo station compared to simulation outputs from UCLALES-SALSA for Case 1 24 September 2020 initialized with an internally mixed aerosol population of dry particles containing 74.5 % v/v organic carbon and 25.5 %v/v sulfate 2020

The effective supersaturation SS_{eff} for droplet activation at equilibrium conditions given was calculated according to the κ-Köhler model of Petters and Kreidenweis (2007) using average D_{50} values from observations and model outputs with a volume fraction weighted average κ-value based on the observed aerosol composition as follows

$$SS_{\text{eff}} = \left(exp\sqrt{\frac{4\left(\frac{4M_w\sigma_w}{RT\rho_w}\right)^3}{27D_{50}^3\kappa}} - 1 \right) \times 100, \tag{11}$$

where M_w, σ_w and ρ_w are the molecular weight of water, the surface tension and density of liquid water at absolute temperature T and atmospheric pressure, and R is the ideal gas constant. Equation (11) is solved with hourly average values of D_{50}.

The average supersaturation at droplet activation as simulated by UCLALES-SALSA was calculated as average weighted values of the maximum supersaturation SS_{max} observed in vertical columns of the model domain driven by updrafts weighted by the cumulative number concentration of activated droplets $N_{d,act}$ as follows

$$SS_{\text{model}} = \sum_x \sum_y \frac{SS_{\max}(x,y) \sum_0^{\text{z-SSmax}} N_{\text{d,act}}}{\sum_0^{z-SSmax} N_{\text{d,act}}} \tag{12}$$

Equation (12) is solved along the cloud domain for hourly intervals.

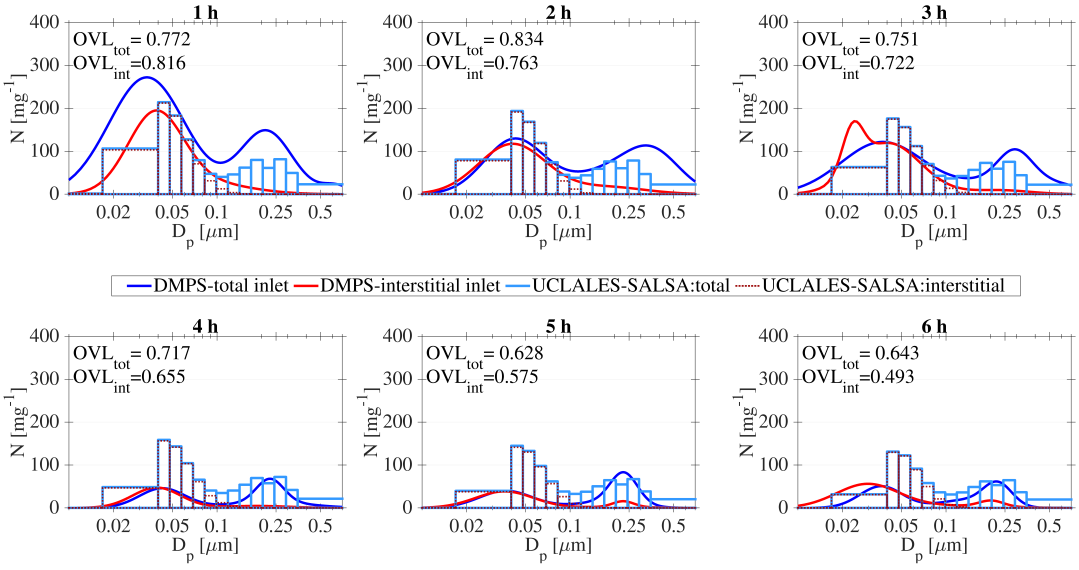

Figure S18. Aerosol size distributions measured with the Twin-inlet DMPS system at the Puijo station compared to simulation outputs from UCLALES-SALSA for Case 2 31 October 2020 initialized with an internally mixed aerosol population of dry particles containing 88 % v/v organic carbon and 12 %v/v sulfate with 40% reduction in the initial aerosol loading without consideration of ice formation (UCLALES-SALSA Level 4)

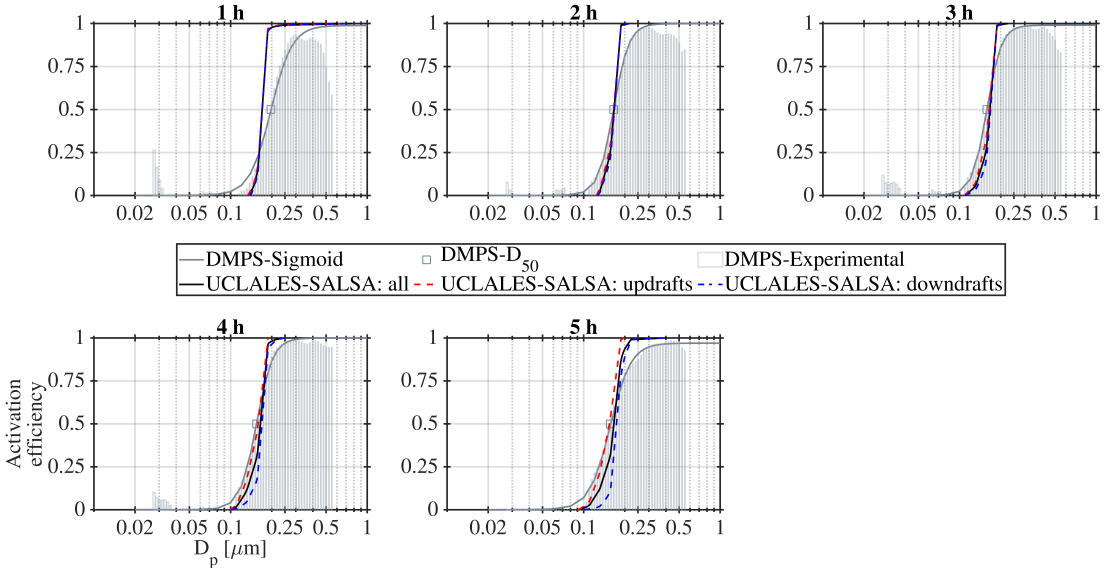

Figure S19. Variability induced by vertical wind in activation efficiency curves for hourly intervals of the cloud event of Case 1 24 September 2020. Observation-based curves are compared to model-based curves in grid points with updrafts or downdrafts at Puijo altitude

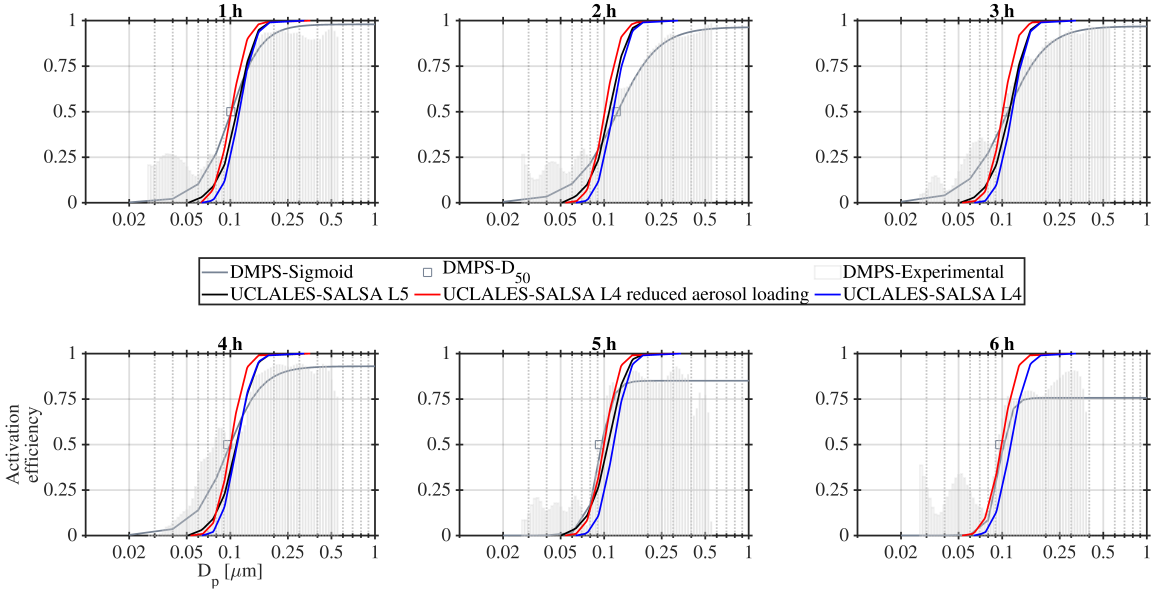

Figure S20. Variability of activation efficiency curves in hourly intervals of the cloud event of Case 2 31 October 2020. Observation-based curves are compared to model-based curves from three different simulations scenarios: UCLALES-SALSA Level 4 no ice formation, UCLALES-SALSA Level 4 no ice formation with 40% reduction in the aerosol loading used for model initialization, UCLALES-SALSA Level 5 with ice formation and 40% reduction in the aerosol loading used for model initialization

9 Model sensitivity analysis to inputs related to aerosol mixing state in simulations of Case 1

Activation efficiency curves can provide valuable information about the processes affecting the droplet formation at cloud base and evaporation within cloud or at the cloud edges. However, in addition, the shape of activation curve is also dependent on the size dependent aerosol hygroscopicity, and therefore of the mixing state of an aerosol population. In a single supersaturation, populations of aerosol particles internally mixed, or existing in a single mixing state show activation curves that can be fitted to a single sigmoid function that plateaus near one; while externally mixed aerosols with two or more mixing states show multiple plateaus with heights less than one that can be fitted to multiple sigmoid functions, each one of them representing the contributions of a different mixing state or the existence of non activated aerosols such as black carbon (e.g. Anttila et al., 2009; Anttila, 2010; Vu et al., 2019).

Since Case 1 occurred during the biomass burning plume period, it is likely to have an externally mixed aerosol population composed of two types of particles, particles locally emitted or formed in situ, and particles from aged biomass burning emissions transported long range. Unfortunately, measurements do not provide information on aerosol mixing state. However, to assess the potential effect of the aerosol chemical diversity in our simulations, we compared the simulation results obtained for an internally mixed aerosol population (74.5 %v/v of organic carbon and 12.5 % v/v of sulphate) with those for an externally mixed aerosol population with the same aerosol number size distribution. In this scenario, 70 % of the total number of particles

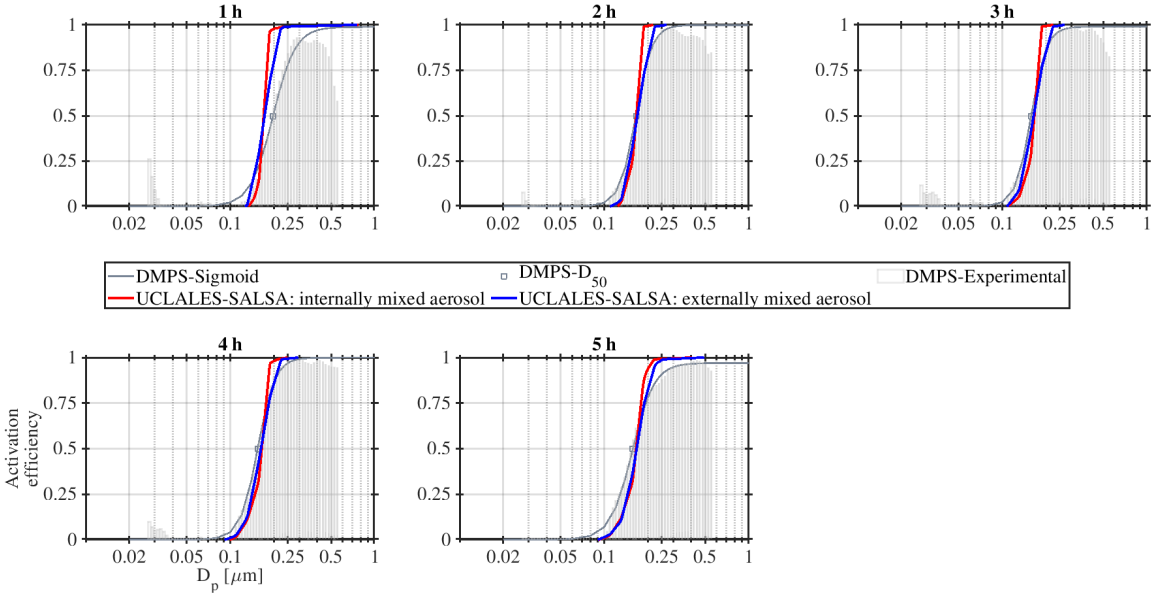

Figure S21. Model variability induced by the aerosol mixing state in activation efficiency curves at Puijo altitude of 225 m for Case 1 24 September 2020

are composed of 65 %v/v of organic carbon and 35 % v/v of sulphate, and the remaining 30% is composed of 97 % v/v organic carbon and 3 %v/v sulphate, qualitatively following the earlier observations from Puijo (Väisänen et al., 2016). Details of aerosol composition calculations are presented in Section D of the supporting information.

The variability induced by the aerosol mixing state in model-based activation efficiency curves is shown in Figure S21. As expected, the slopes in activation efficiency curves of the externally mixed aerosol population are less steep than those for the internally mixed aerosol, and therefore, there is a better correspondence to the measured activation efficiency curves for particle sizes above D_{50}. However, without a better knowledge of aerosol mixing state, we can not conclude if the better match with observed slope of activation curve is actually because of externally mixed aerosol, or if the model representation of entrainment mixing at the cloud top could be improved. Nevertheless, there are no significant changes in D_{50} values neither significant improvements in the model description of the activation of smaller particles with sizes below D_{50}. Vertical profiles of average total droplet number concentrations show a slight decrease of 5-8 % when the simulation is initialized with an externally mixed aerosol population. Changes in droplet size distributions are negligible as discussed later in Figure S22.

10 Cloud microphysics and derived quantities

Droplet size distributions at the Puijo station were measured in the size range of 3 µm–50 µm with 30 bins with a fog droplet spectrometer (FM-100, Droplet Measurement Technologies, USA) (Spiegel et al., 2012). Number concentrations and size

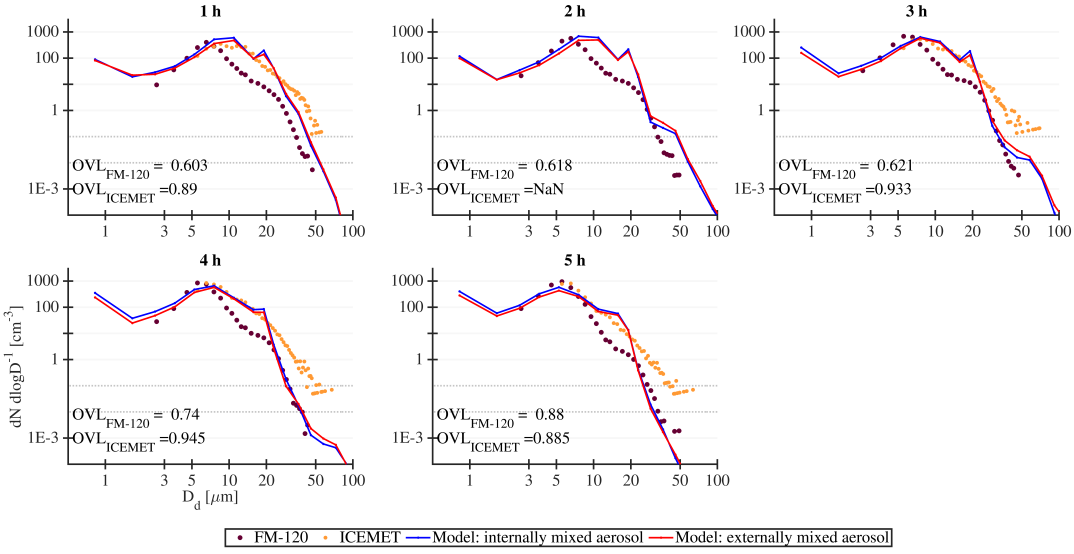

Figure S22. Variability of modeled droplet size distributions of Case 1 24 September 2020 caused by variation of the aerosol mixing state. OVL values for the modeled distribution with the simulation scenario with internally mixed aerosol. Droplet size distributions measured with the fog monitor (FM-120) and the holographic imaging system (ICEMET) at the Puijo station compared to model outputs from UCLALES-SALSA.

distributions including larger droplets and ice particles were measured with a holographic imaging system (Optical cloud droplet and ice crystal measurement system ICEMET, icing condition evaluation method, University of Oulu, Finland) in the range of 5 µm–200 µm with 195 bins (Kaikkonen et al., 2020). We used the overlapping index to measure the similarity or agreement between the droplet size distributions calculated with the model and those observed by our instruments. Values for Case 1 are reported directly into Figure S22, and in Table S5 for Case 2.

Overlapping index values for our studied cases indicate a moderate agreement between modeled and observed droplet size distributions that ranges from 0.430 to 0.811. This degree of closure must be analyzed carefully since any of the instruments could provide a complete scanning along the droplet size range found in our simulations (i.e. 1 µm<D<2000 µmm). Observational ranges are 3 µm-50 µm and 5 µm–200 µm for the FM-120 and the ICEMET, respectively. In case 1, where cloud formation occurred with high aerosol loadings, droplet number concentrations in the size range between 1 µm- 5 µm dominated the droplet spectra. Since these small cloud droplets were not efficiently detected, neither by the FM-120 nor by the ICEMET, negative biases from real concentrations were inevitable. On the contrary, during case 2, cloud formation occurred with low aerosol loadings, larger droplets could not be efficiently accounted for in the FM-120 that was also affected by anisoaxial conditions, and the ICEMET could not detect the largest sizes because of very low number concentrations. A more detailed analysis of the performance of these instruments during the Puijo 2020 campaign was presented by Tiitta et al. (2022).

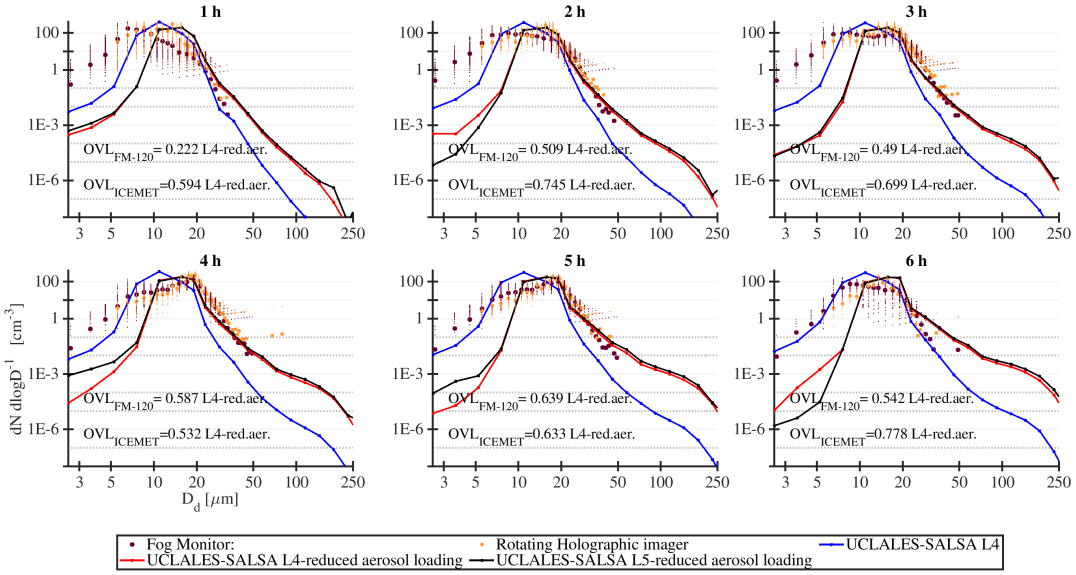

Figure S23. Variability of modeled droplet size distributions of Case 2 31 October 2020 caused by the reduction in the initial aerosol loading and by the consideration of ice formation. Droplet size distributions measured with the fog monitor (FM-120) and the holographic imaging system (ICEMET) at the Puijo station compared to model outputs from UCLALES-SALSA. OVL values for the modeled distribution from the simulation scenario with reduced aerosol loading no ice formation

11 Emulation of the radar Doppler velocity

Doppler radars detect motion by measuring the phase shift of microwaves caused by interaction with falling objects (e.g. hydrometeors). The Doppler velocity represents the component of hydrometeor velocity in the direction of the radar beam and therefore it is the vector sum of its settling velocity and the air velocity itself(Stull, 2017). When the sampling volume contains a population of hydrometeors, the observed Doppler velocity corresponds to the average settling velocity of all droplets falling through the turbulent air, and thus, represents the scattering properties of the droplet distribution (Frisch et al., 1995).

The scattering properties of the droplet distribution are expressed by the radar reflectivity η or backscattering cross section per unit of volume. It accounts for the incremental scattering contributions of all droplets in the sampling volume assuming that light extinction occurs in the Rayleigh scattering regime as follows

$$\eta = \int \frac{\partial \eta}{\partial D} dD = \int \sigma_{\text{ext}} n(D)\, dD = \int \frac{\lambda^2}{\pi} \left(\frac{\pi D}{\lambda}\right)^6 \left|\frac{m^2-1}{m^2+2}\right|^2 n(D)\, dD = \int \pi^5 \lambda^{-4} \frac{2}{3} \left|\frac{m^2-1}{m^2+2}\right|^2 D^6 n(D)\, dD, \quad (13)$$

where λ is the radar wavelength, σ_{ext} is the backscatterring cross section of a droplet and m is the complex refractive index of water (Battan, 1973; Frisch et al., 1995).

Table S5. Overlapping indexes of observed droplet size distributions in hourly intervals during Case 2 of 31 October 2020. L4: base scenario with no ice formation, L4: simulation scenario with 40% reduction in the aerosol loading used in model initialization without ice formation and related processes, L5: simulation scenario with 40% reduction in the aerosol loading including ice formation and related processes.

Hour	L4	L4-reduced aerosol loading	L5-ice formation
Fog monitor FM-120			
1	0.351	0.222	0.222
2	0.614	0.509	0.512
3	0.585	0.490	0.503
4	0.516	0.587	0.606
5	0.558	0.639	0.659
6	0.723	0.542	0.520
Mean $\pm$ standard deviation	0.558 ± 0.123	0.498$\pm$0.146	0.504$\pm$0.151
Holographic imaging system, ICEMET			
1	0.706	0.594	0.594
2	0.631	0.745	0.750
3	0.626	0.699	0.712
4	0.356	0.532	0.551
5	0.418	0.633	0.653
6	0.710	0.778	0.756
Mean $\pm$ standard deviation	0.574 ± 0.151	0.664$\pm$0.094	0.669$\pm$0.085

Nevertheless, η is not measured directly, instead it is correlated to the radar reflectivity factor Z or its analog dBZ as follows

$$\eta = \int \frac{\partial \eta}{\partial D} dD = \pi^5 \lambda^{-4} |K|^2 Z, \tag{14}$$

where the term ${}^{m^2-1}/_{m^2+2}$ is referred as the dielectric factor K that depends on wavelength, temperature and density in case of ice particles (i.e.$K^2 = 0.93 \pm 0.004$ for liquid water at temperature between 273 K and 293 K at the wavelength band between 3 cm and 10 cm) (Battan, 1973), and the variable Z is the radar reflectivity factor or the sixth statistical moment of the droplet size distribution expressed as

$$Z = \int D^6 n(D)\, dD. \tag{15}$$

The Doppler velocity V is inferred from the relation between η and Z because the backscattering contribution ${}^{\partial \eta}/_{\partial D}$ depends the hydrometeor settling velocity V_s. The Doppler velocity is the reflectivity-weighted velocity distribution calculated as

$$V = \eta^{-1} \int V \frac{\partial \eta}{\partial V} dV = \eta^{-1} \int V_s(D) \frac{\partial \eta}{\partial D} dD = \frac{\int V_s(D) \pi^5 \lambda^{-4} |K|^2 D^6 n(D)\, dD}{\pi^5 \lambda^{-4} |K|^2 Z} = \frac{\int V_s(D) D^6 n(D)\, dD}{\int D^6 n(D)\, dD}. \tag{16}$$

If there are different types of hydrometeors (i.e. cloud droplets, drizzle, ice particles) the Doppler velocity is the mean reflectivity-weighted velocity distribution (Kollias et al., 2011) calculated as

$$V = \frac{V_{\rm cloud} Z_{\rm cloud} + V_{\rm drizzle} Z_{\rm drizzle} + V_{\rm ice} Z_{\rm ice}}{Z_{\rm cloud} + Z_{\rm drizzle} + Z_{\rm ice}}, \tag{17}$$

In this study, we knew the Doppler velocity retrieved from measurements of the cloud radar located at the Savilahti station, our goal was to use model-based droplet number concentrations and hydrometeor sizes to emulate its value using Eq. (16).

First, we calculate the sedimentation velocity of the droplet spectrum using modeled wet size of our hydrometeors. Settling velocities for liquid droplets were calculated via Davies number in terms of the Reynolds number (Hinds, 1999) while for ice particles we used the shape-dependent parametrization of Khvorostyanov and Curry (2000) assuming crystals with sector-like branches.

Then, we calculate the zero-th and sixth moments of the sedimentation velocity using number concentrations and wet sizes of cloud droplets, drizzle and ice particles to find the radar reflectivity, Eq. (15) and the doppler velocity (16) for each type of hydrometeors inside the cloud.

Finally, we emulate the radar velocity by adding the reflectivity weighted Doppler velocity of the hydrometeor spectrum to the modeled vertical wind that includes turbulence effects (Frisch et al., 1995; Kollias et al., 2011). The emulated Doppler velocity is calculated as

$$V_e = V + w_{\rm wind}, \tag{18}$$

where V is given by Eq. (16) and $w_{\rm wind}$ is the vertical component of the wind velocity as calculated by UCLALES-SALSA.

As we did before, we used the overlapping index OVL which measures the agreement or similarity between two probability distributions (Inman and Bradley Jr., 1989) to measure the modelling closure of the radar velocity distributions. this time, our variable x is the radar velocity and $p_1(x)$ and $p_2(x)$ are probability distributions of radar velocity based on observations and modeled by UCLALES-SALSA, respectively.

Table S6. Overlapping indexes of the emulated and observed radar velocity distributions in hourly intervals during Case 2 of 31 October 2020. L4: base scenario with no ice formation, L4: simulation scenario with 40% reduction in the aerosol loading used in model initialization without ice formation and related processes, L5: simulation scenario without reduction of the aerosol loading used in model initialization but including ice formation and related processes.

Hour	L4	L4-reduced aerosol loading	L5-ice formation and reduced aerosol loading
1	0.8000	0.7780	0.7262
2	0.7481	0.7915	0.9074
3	0.8467	0.9434	0.8183
4	0.7043	0.8164	0.9079
5	0.6773	0.8359	0.9247
6	0.6183	0.7984	0.8886
Mean $\pm$ Standard deviation	0.7325 ± 0.083	0.8273 ± 0.0604	0.8622 ± 0.0764

References

Ács, F., Mihailovića, D. T., and Rajkovićb, B.: A Coupled Soil Moisture and Surface Temperature Prediction Model, Journal of Applied Meteorology and Climatology, 30, 812–822, https://doi.org/10.1175/1520-0450(1991)030<0812:ACSMAS>2.0.CO;2, 1991.

Ahola, J., Korhonen, H., Tonttila, J., Romakkaniemi, S., Kokkola, H., and Raatikainen, T.: Modelling mixed-phase clouds with the large-eddy model UCLALES–SALSA, Atmospheric Chemistry and Physics, 20, 11 639–11 654, https://doi.org/10.5194/acp-20-11639-2020, 2020.

Anttila, T.: Sensitivity of cloud droplet formation to the numerical treatment of the particle mixing state, Journal of Geophysical Research, 115, D21 205, https://doi.org/10.1029/2010JD013995, 2010.

Anttila, T., Vaattovaara, P., Komppula, M., Hyvärinen, A.-P., Lihavainen, H., Kerminen, V.-M., and Laaksonen, A.: Size-dependent activation of aerosols into cloud droplets at a subarctic background site during the second Pallas Cloud Experiment (2nd PaCE): method development and data evaluation, Atmospheric Chemistry and Physics, 9, 4841–4854, https://doi.org/10.5194/acp-9-4841-2009, 2009.

Balkanski, Y., Schulz, M., Claquin, T., and Guibert, S.: Reevaluation of Mineral aerosol radiative forcings suggests a better agreement with satellite and AERONET data, Atmospheric Chemistry and Physics, 7, 81–95, https://doi.org/10.5194/acp-7-81-2007, 2007.

Battan, L. J.: Radar Observation of the Atmosphere, The University of Chicago Press, Ltd., Chicago, US, 1973.

Bühl, J., Leinweber, R., Görsdorf, U., Radenz, M., Ansmann, A., and Lehmann, V.: Combined vertical-velocity observations with Doppler lidar, cloud radar and wind profiler, Atmospheric Measurement Techniques, 8, 3527–3536, https://doi.org/10.5194/amt-8-3527-2015, 2015.

DeCarlo, P. F., Slowik, J. G., Worsnop, D. R., Davidovits, P., and Jimenez, J. L.: Particle morphology and density characterization by combined mobility and aerodynamic diameter measurements. Part 1: Theory, Aerosol Science and Technology, 38, 1185–1205, https://doi.org/10.1080/027868290903907, 2004.

DeCarlo, P. F., Kimmel, J. R., Trimborn, A., Northway, M. J., Jayne, J. T., Aiken, A. C., Gonin, M., Fuhrer, K., Horvath, T., Docherty, K. S., Worsnop, D. R., and Jimenez, J. L.: Field-deployable, high-resolution, time-of-flight aerosol mass spectrometer, Analytical Chemistry, 78, 8281–8289, https://doi.org/10.1021/ac061249n, 2006.

Frisch, A. S., Fairall, C. W., and Snider, J. B.: Measurement of Stratus Cloud and Drizzle Parameters in ASTEX with a K-alpha-Band Doppler Radar and a Microwave Radiometer, Journal of Atmospheric Sciences, 52, 2788–2799, https://doi.org/10.1175/1520-0469(1995)052<2788:MOSCAD>2.0.CO;2, 1995.

Hinds, W. C.: Aerosol technology : properties, behavior, and measurement of airborne particles, Wiley, 1999.

Hirsikko, A., O'Connor, E. J., Komppula, M., Korhonen, K., Pfüller, A., Giannakaki, E., Wood, C. R., Bauer-Pfundstein, M., Poikonen, A., Karppinen, T., Lonka, H., Kurri, M., Heinonen, J., Moisseev, D., Asmi, E., Aaltonen, V., Nordbo, A., Rodriguez, E., Lihavainen, H., Laaksonen, A., Lehtinen, K. E. J., Laurila, T., Petäjä, T., Kulmala, M., and Viisanen, Y.: Observing wind, aerosol particles, cloud and precipitation: Finland's new ground-based remote-sensing network, Atmospheric Measurement Techniques, 7, 1351–1375, https://doi.org/10.5194/amt-7-1351-2014, 2014.

Hoose, C., Kristjánsson, J. E.and Chen, J., and Hazra, A.: A classical-theory-based parameterization of heterogeneous ice nucleation by mineral dust, soot, and biological particles in a Global Climate Model, Journal of Atmospheric Sciences, 67, 2483–2503, https://doi.org/10.1175/2010JAS3425.1, 2010.

Hu, M., Peng, J., Sun, K., Yue, D., Guo, S., Wiedensohler, A., and Wu, Z.: Estimation of Size-Resolved Ambient Particle Density Based on the Measurement of Aerosol Number, Mass, and Chemical Size Distributions in the Winter in Beijing, Environmental Science & Technology, 46, 9941–9947, https://doi.org/10.1021/es204073t, 2012.

Inman, H. F. and Bradley Jr., E. L.: The overlapping coefficient as a measure of agreement between probability distributions and point estimation of the overlap of two normal densities, Communications in Statistics - Theory and Methods, 18, 3851–3874, https://doi.org/10.1080/03610928908830127, 1989.

Jacobson, M. Z.: Fundamentals of atmospheric modeling, Cambridge University Press, New York, 2nd edn., 2005.

Kaikkonen, V. A., Molkoselkä, E. O., and Mäkynen, A. J.: A rotating holographic imager for stationary cloud droplet and ice crystal measurements, Optical Review, 27, 205–216, https://doi.org/10.1007/s10043-020-00583-y, 2020.

Khvorostyanov, V. and Sassen, K.: Toward the theory of homogeneous nucleation and its parameterization for cloud models, Geophysical Research Letters, 25, 3155–3158, https://doi.org/https://doi.org/10.1029/98GL02332, 1998.

Khvorostyanov, V. I. and Curry, J. A.: A new theory of heterogeneous ice nucleation for application in cloud and climate models, Geophysical Research Letters, 27, 4081–4084, https://doi.org/https://doi.org/10.1029/1999GL011211, 2000.

Kokkola, H., Korhonen, H., Lehtinen, K. E. J., Makkonen, R., Asmi, A., Järvenoja, S., Anttila, T., Partanen, A.-I., Kulmala, M., Järvinen, H., Laaksonen, A., and Kerminen, V.-M.: SALSA: a Sectional Aerosol module for Large Scale Applications, Atmospheric Chemistry and Physics, 8, 2469–2483, https://doi.org/10.5194/acp-8-2469-2008, 2008.

Kollias, P., Rémillard, J., Luke, E., and Szyrmer, W.: Cloud radar Doppler spectra in drizzling stratiform clouds: 1. Forward modeling and remote sensing applications, Journal of Geophysical Research: Atmospheres, 116, https://doi.org/https://doi.org/10.1029/2010JD015237, 2011.

Küchler, N., Kneifel, S., Löhnert, U., Kollias, P., Czekala, H., and Rose, T.: A W-Band Radar–Radiometer System for Accurate and Continuous Monitoring of Clouds and Precipitation, Journal of Atmospheric and Oceanic Technology, 34, 2375–2392, https://doi.org/10.1175/JTECH-D-17-0019.1, 2017.

Linstrom, P. J. and Eds., W. G. M.: NIST Chemistry WebBook, NIST Standard Reference Database Number 69, Gaithersburg: National Institute of Standards and Technology, http://webbook.nist.gov/chemistry, 2017.

Mahowald, N., Albani, S., Kok, J. F., Engelstaeder, S., Scanza, R., Ward, D. S., and Flanner, M. G.: The size distribution of desert dust aerosols and its impact on the Earth system, Aeolian Research, 15, 53–71, https://doi.org/https://doi.org/10.1016/j.aeolia.2013.09.002, 2014.

Manninen, A. J., Marke, T., Tuononen, M., and O'Connor, E. J.: Atmospheric Boundary Layer Classification With Doppler Lidar, Journal of Geophysical Research: Atmospheres, 123, 8172–8189, https://doi.org/https://doi.org/10.1029/2017JD028169, 2018.

Markowicz, K. M., Flatau, P. J., Kardas, A. E., Remiszewska, J., Stelmaszczyk, K., and Woeste, L.: Ceilometer Retrieval of the Boundary Layer Vertical Aerosol Extinction Structure, Journal of Atmospheric and Oceanic Technology, 25, 928 – 944, https://doi.org/10.1175/2007JTECHA1016.1, 2008.

Ng., N. L., Herndon, S. C., Trimborn, A., Canagaratna, M. R., Croteau, P. L., Onasch, T. B., Sueper, D., Worsnop, D. R., Zhang, Q., Sun, Y. L., and T.J., J.: An Aerosol Chemical Speciation Monitor (ACSM) for Routine Monitoring of the Composition and Mass Concentrations of Ambient Aerosol, Aerosol Science and Technology, 45, 780–794, https://doi.org/10.1080/02786826.2011.560211, 2011.

Parshintsev, J., Hartonen, K., and Riekkola, M.-L.: Chapter 24 - Environmental analysis: Atmospheric samples, in: Liquid Chromatography (Second Edition), edited by Fanali, S., Haddad, P. R., Poole, C. F., and Riekkola, M.-L., pp. 769–798, Elsevier, second edi edn., https://doi.org/https://doi.org/10.1016/B978-0-12-805392-8.00024-4, 2017.

Petters, M. D. and Kreidenweis, S. M.: A single parameter representation of hygroscopic growth and cloud condensation nucleus activity, Atmospheric Chemistry and Physics, 7, 1961–1971, https://doi.org/10.5194/acp-7-1961-2007, 2007.

Portin, H., Leskinen, A., Hao, L., Kortelainen, A., Miettinen, P., Jaatinen, A., Laaksonen, A., Lehtinen, K. E. J., Romakkaniemi, S., and Komppula, M.: The effect of local sources on particle size and chemical composition and their role in aerosol–cloud interactions at Puijo measurement station, Atmospheric Chemistry and Physics, 14, 6021–6034, https://doi.org/10.5194/acp-14-6021-2014, 2014.

Portin, H. J., Komppula, M., Leskinen, A. P., Romakkaniemi, S., Laaksonen, A., and Lehtinen, K. E. J.: Observations of aerosol–cloud interactions at the Puijo semi-urban measurement station, Boreal Environmental Research, 14, 641–653, http://www.borenv.net/BER/archive/ber144.htm, 2009.

Rocha-Lima, A., Martins, J. V., Remer, L. A., Todd, M., Marsham, J. H., Engelstaedter, S., Ryder, C. L., Cavazos-Guerra, C., Artaxo, P., Colarco, P., and Washington, R.: A detailed characterization of the Saharan dust collected during the Fennec campaign in$\sim$2011: in situ ground-based and laboratory measurements, Atmospheric Chemistry and Physics, 18, 1023–1043, https://doi.org/10.5194/acp-18-1023-2018, 2018.

Royal Society of Chemistry, R.: ChemSpider. Search and Share Chemistry, http://www.chemspider.com/, 2015.

Samaké, A., Jaffrezo, J.-L., Favez, O., Weber, S., Jacob, V., Canete, T., Albinet, A., Charron, A., Riffault, V., Perdrix, E., Waked, A., Golly, B., Salameh, D., Chevrier, F., Oliveira, D. M., Besombes, J.-L., Martins, J. M. F., Bonnaire, N., Conil, S., Guillaud, G., Mesbah, B., Rocq, B., Robic, P.-Y., Hulin, A., Le Meur, S., Descheemaecker, M., Chretien, E., Marchand, N., and Uzu, G.: Arabitol, mannitol, and glucose as tracers of primary biogenic organic aerosol: the influence of environmental factors on ambient air concentrations and spatial distribution over France, Atmospheric Chemistry and Physics, 19, 11 013–11 030, https://doi.org/10.5194/acp-19-11013-2019, 2019.

Simoneit, B. R. T., Schauer, J. J., Nolte, C. G., Oros, D. R., Elias, V. O., Fraser, M. P., Rogge, W. F., and Cass, G. R.: Levoglucosan, a tracer for cellulose in biomass burning and atmospheric particles, Atmospheric Environment, 33, 173–182, https://doi.org/https://doi.org/10.1016/S1352-2310(98)00145-9, 1999.

Spiegel, J. K., Zieger, P., Bukowiecki, N., Hammer, E., Weingartner, E., and Eugster, W.: Evaluating the capabilities and uncertainties of droplet measurements for the fog droplet spectrometer (FM-100), Atmospheric Measurement Techniques, 5, 2237–2260, https://doi.org/10.5194/amt-5-2237-2012, 2012.

Stokes, R. H. and Robinson, R. A.: Interactions in Aqueous Nonelectrolyte Solutions. I. Solute-Solvent Equilibria, The Journal of Physical Chemistry, 70, 2126–2131, https://doi.org/10.1021/j100879a010, 1966.

Stull, R.: Practical Meteorology: An Algebra-based Survey of Atmospheric Science, The University of British Columbia, 1.02b edn., 2017.

Tiitta, P., Leskinen, A., Kaikkonen, V., Molkoselkä, E., Mäkynen, A., Joutsensaari, J., Calderon, S., Romakkaniemi, S., and Komppula, M.: Intercomparison of holographic imaging and single-particle forward light scattering in-situ measurements of liquid clouds in changing atmospheric conditions, Atmospheric Measurement Techniques Discussions, 2022, 1–20, https://doi.org/10.5194/amt-2021-423, 2022.

Tonttila, J., Maalick, Z., Raatikainen, T., Kokkola, H., Kühn, T., and Romakkaniemi, S.: UCLALES–SALSA v1.0: a large-eddy model with interactive sectional microphysics for aerosol, clouds and precipitation, Geoscientific Model Development, 10, 169–188, https://doi.org/10.5194/gmd-10-169-2017, 2017.

Tonttila, J., Afzalifar, A., Kokkola, H., Raatikainen, T., Korhonen, H., and Romakkaniemi, S.: Precipitation enhancement in stratocumulus clouds through airborne seeding: sensitivity analysis by UCLALES-SALSA, Atmospheric Chemistry and Physics, 21, 1035–1048, https://doi.org/10.5194/acp-21-1035-2021, 2021.

Tucker, S. C., Senff, C. J., Weickmann, A. M., Brewer, W. A., Banta, R. M., Sandberg, S. P., Law, D. C., and Hardesty, R. M.: Doppler Lidar Estimation of Mixing Height Using Turbulence, Shear, and Aerosol Profiles, Journal of Atmospheric and Oceanic Technology, 26, 673 – 688, https://doi.org/10.1175/2008JTECHA1157.1, 2009.

Väisänen, O., Ruuskanen, A., Ylisirniö, A., Miettinen, P., Portin, H., Hao, L., Leskinen, A., Komppula, M., Romakkaniemi, S., Lehtinen, K. E. J., and Virtanen, A.: In-cloud measurements highlight the role of aerosol hygroscopicity in cloud droplet formation, Atmospheric Chemistry and Physics, 16, 10 385–10 398, https://doi.org/10.5194/acp-16-10385-2016, 2016.

Vu, D., Gao, S., Berte, T., Kacarab, M., Yao, Q., Vafai, K., and Asa-Awuku, A.: External and internal cloud condensation nuclei (CCN) mixtures: controlled laboratory studies of varying mixing states, Atmospheric Measurement Techniques, 12, 4277–4289, https://doi.org/10.5194/amt-12-4277-2019, 2019.

Wood, R.: Stratocumulus Clouds, Monthly Weather Review, 140, 2373–2423, https://doi.org/10.1175/MWR-D-11-00121.1, 2012.